J. Iron Steel Res. Int. (2021) 28:1463–1470
https://doi.org/10.1007/s42243-021-00585-3

ORIGINAL PAPER

Twinning induced remarkable strain hardening in a novel $Fe_{50}Mn_{20}Cr_{20}Ni_{10}$ medium entropy alloy

Ming-jie Qin[1] · **Xi Jin**[1] · **Min Zhang**[1] · **Hui-jun Yang**[1,2] · **Jun-wei Qiao**[1,2,3]

Received: 6 July 2020 / Revised: 31 August 2020 / Accepted: 3 September 2020 / Published online: 13 April 2021
© China Iron and Steel Research Institute Group 2021

Abstract

The microstructures and tension properties of $Fe_{50}Mn_{20}Cr_{20}Ni_{10}$ medium entropy alloy (MEA) were investigated, which was produced by vacuum induction melting and subsequently was homogenized at 1200 °C for 6 h. Microstructure characterization shows the single-phase solid solution with face-centered cubic structure by means of transmission electron microscopy and scanning electron microscopy combined with energy disperse spectroscopy. Our Fe-MEA has an ultimate tensile strength of 550 ± 10 MPa and a high strain hardening exponent, n, of 0.41 as well as a higher ductility (60%) than those of CrMnFeCoNi alloy. The single-phase solid solution deforms plastically via dislocations and twins. Twin boundaries associated with deformation twinning impede dislocation motion, enhancing the strain hardening capacity. This article focuses on the insights into the concept of Fe-MEAs and provides a potential direction for the future development of high entropy alloys and MEAs.

Keywords Medium entropy alloy · Alloy design · Labusch model · Twinning induced plasticity · Strain hardening

1 Introduction

Conventional alloys usually contain only one or two primary elements, with small amounts of alloying elements added to enhance specific physical and/or mechanical properties. In contrast, medium and high entropy alloys (MEAs and HEAs) consist of at least four principal elements with approximately equal proportions [1–3]. The increased number of elements not only greatly expands possible alloy composition spaces and potential for promising new alloys [4] but also leads to excellent mechanical properties [5–9] with a good combination of strength, ductility and toughness at room temperature and cryogenic temperatures.

A representative example is the equiatomic FeCoCrMnNi HEA, and under quasi-static uniaxial tensile loading, the room-temperature mechanical performances of FeCoCrMnNi HEA are super to those of simple binary Fe–Mn alloys [10]. On the other hand, Gludovatz et al. [11] recently reported that the mechanical performance of equiatomic FeCoCrMnNi alloy is better than that of all conventional alloys under cryogenic conditions. The fracture toughness values measured by compact tension test at cryogenic temperatures down to 77 K were found to exceed 200 MPa $m^{1/2}$ at crack initiation and 300 MPa $m^{1/2}$ for stable crack growth. The potential deformation mechanism that is associated with these excellent properties is owing to nano-twins, which is absent at ambient temperatures [12]. Generally, the deformation mechanisms and stacking fault energy (SFE) have the following relationships in high manganese twinning induced plasticity (TWIP) steels: (i) the dislocation slip with SFEs larger than 60 mJ m^{-2}; (ii) the twinning with SFEs between 20 and 60 mJ m^{-2}; and (iii) transformation from face-centered cubic (FCC) to hexagonal close-packed phase, i.e., transformation induced plasticity (TRIP), with SFEs lower than 20 mJ m^{-2} [13–16].

✉ Jun-wei Qiao
qiaojunwei@gmail.com

[1] College of Materials Science and Engineering, Taiyuan University of Technology, Taiyuan 030024, Shanxi, China

[2] Key Laboratory of Interface Science and Engineering in Advanced Materials, Ministry of Education, Taiyuan University of Technology, Taiyuan 030024, Shanxi, China

[3] State Key Laboratory of Explosion Science and Technology, Beijing Institute of Technology, Beijing 100081, China

In this study, we purposefully designed non-equiatomic FCC-based MEAs with four principle elements (i.e., Fe, Mn, Cr and Ni) and successfully developed a non-equiatomic FCC $Fe_{50}Mn_{20}Cr_{20}Ni_{10}$ MEA using an appropriate adjustment of composition ratio to decrease SFE in order to promote twinning and reduce the cost of alloy. The designed $Fe_{50}Mn_{20}Cr_{20}Ni_{10}$ MEA shows dislocation and twinning co-dominated deformation mechanism. The effect of SFE on the deformation mode is discussed in detail. This work provides a guide for the design of high-performance and low-cost second-generation Fe-MEAs or HEAs for extensive applications.

2 Experimental

An $Fe_{50}Mn_{20}Cr_{20}Ni_{10}$ MEA was fabricated using a vacuum induction melting equipment under an argon atmosphere using commercial pure elements (the purity of each raw material was 99.9% at least). Raw materials were alloyed in a boron nitride crucible to make a master alloy of 350 g in weight. Additional 5 wt.% Mn was added to compensate for the loss of Mn by evaporation during melting. The master alloy was molten and poured into rectangular copper molds (length of 30 mm, width of 30 mm, and thickness of 100 mm). The alloys were re-melted twice to ensure chemical homogeneity and were homogenized at 1200 °C for 6 h. The phase structure was characterized by X-ray diffraction (XRD) using a Rigaku UltimalV diffractometer. Transmission electron microscopy (TEM) observations were performed using a JEM-F200 microscope operating at 200 kV. Scanning electron microscope (SEM) was operated at 20 kV and a sample tilt of 70°. The tensile samples with gauge length of 10 mm and width of 3 mm were cut into a dog-bone shape using the electrical discharge machine. Tensile tests were carried out at a strain rate of $1 \times 10^{-3}\ s^{-1}$ using an Instron 5969 materials testing machine at room temperature (293 K).

3 Results and discussion

3.1 Design strategy of a novel Fe-MEA

The alloy design strategy is based on the following considerations: (i) as reported elsewhere [17], SFE of the equiatomic FeMnNiCoCr HEA was determined to be 25 mJ/m^2 using a combination of density functional theory calculations and XRD experiments. Reducing Ni and Co contents would lower SFE and alloying costs and increase the potential industrial applicability of the alloys. (ii) It is well known that stainless steels have good corrosion resistance because of the addition of a large number of alloying elements including Cr [18]. And (iii) as recently reported in Ref. [19], $Fe_{40}Mn_{20}Cr_{20}Ni_{20}$ MEA exhibits deformation nano-twins at cryogenic temperatures. Nevertheless, it is absent at ambient temperature. Thus, to avoid the brittle sigma phase, reduce cost and achieve TWIP effect in a single FCC phase microstructure, $Fe_{50}Mn_{20}Cr_{20}Ni_{10}$ alloy with reduced Ni content and Co totally removed is developed.

As shown in Table 1, some thermodynamic parameters of the present alloy have been calculated, including the mixed entropy (ΔS_{mix}), mixing enthalpy (ΔH_{mix}), misfit of atomic radius (δ), electronegativity difference ($\Delta\chi$) and valance electron concentration (VEC). Table 1 suggests that these parameters all meet the phase formation criterion and are beneficial to obtaining simple FCC solid solutions.

Table 1 Calculated parameters of $Fe_{50}Mn_{20}Cr_{20}Ni_{10}$ and HEA phase formation criteria [34, 35]

Parameter	ΔS_{mix}	ΔH_{mix}/(kJ mol^{-1})	δ/%	VEC	$\Delta\chi$
Alloy	10.14	−1.68	3.994	7.6	0.124
Criterion		(−15)–(+5)	≤ 6.6		

3.2 Microstructure

Figure 1a shows SEM image of the homogenized $Fe_{50}Mn_{20}Cr_{20}Ni_{10}$ MEA, which was composed of fully recrystallized equiaxed grains with an average grain size of ~ 100 µm. And it can be concluded that the crystal orientations were random without any texture. A region containing a normal grain boundary (GB) of the homogenized alloy was prepared for compositional homogeneity analysis by energy-dispersive spectrum (EDS), as shown in Fig. 1b. The accurate composition of the homogenized alloy was obtained by conducting a comprehensive chemical analysis and the results are listed in Table 2. All the alloying elements (Fe, Mn, Cr and Ni) were homogenously distributed without apparent elemental segregation or secondary phases, indicating that Fe-based MEA has a uniform microstructure and is a random solid solution. This is different from FeMn- and FeMnNi-based alloys in which Mn segregation at GBs is usually found [20–22]. Figure 2 exhibits XRD patterns of the homogenized sample, which indicates that the present alloy has single-phase FCC structure, i.e., an austenite-type structure. Moreover, a_γ is the austenite lattice parameter that can be calculated as to be 0.365 nm by the following equation:

$$a_\gamma = d_{hkl} \times \sqrt{h^2 + k^2 + l^2} \tag{1}$$

where d_{hkl} is the inter-planar spacing at austenite

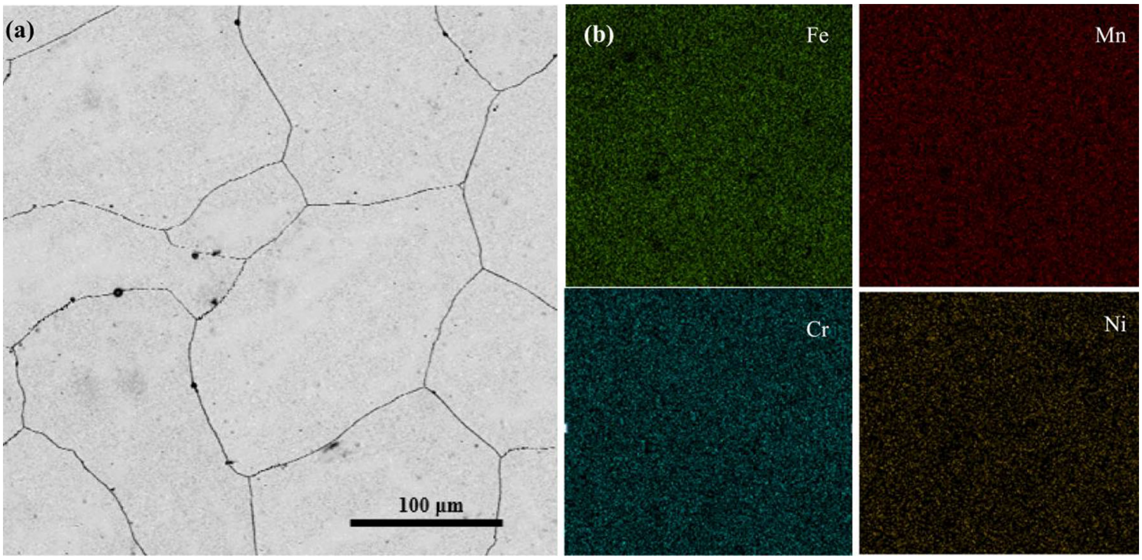

Fig. 1 Microstructures and compositional distributions in $Fe_{50}Mn_{20}Cr_{20}Ni_{10}$ alloy. **a** SEM image of homogenized sample; **b** SEM–EDS maps showing homogeneous distributions of Fe, Mn, Cr and Ni elements

Table 2 Chemical composition of $Fe_{50}Mn_{20}Cr_{20}Ni_{10}$ alloy as determined by SEM–EDS analysis (at.%)

Element	Fe	Mn	Cr	Ni
Grains	50.6 ± 0.6	20.7 ± 0.3	19.4 ± 0.3	9.3 ± 0.2
Alloy composition	50.9 ± 1.2	20.6 ± 0.5	18.8 ± 0.6	9.7 ± 0.3

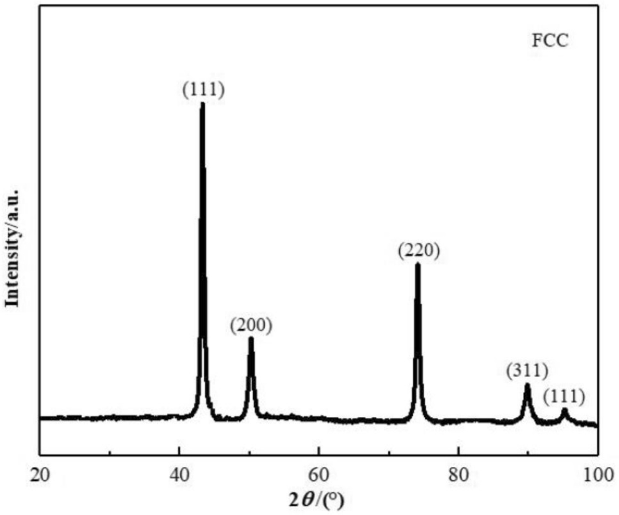

Fig. 2 XRD patterns of homogenized sample. 2θ Diffraction angle

reflections $\{hkl\}$. d_{hkl} is related to the angular position (θ_{hkl}) and X-ray wavelength (λ) as follows:

$$d_{hkl} = \lambda/2\sin\theta_{hkl} \tag{2}$$

3.3 Mechanical properties at room temperature

Figure 3 shows the tensile stress–strain and strain hardening rate curves of $Fe_{50}Mn_{20}Cr_{20}Ni_{10}$ MEA at room temperature. The alloy has a yield strength of 300 ± 10 MPa, an ultimate tensile strength of 550 ± 10 MPa and tensile ductility of 60% ± 5%, which are comparable to those of CrMnFeCoNi [11, 23], CrMnFeCo [6, 24–26] and CrFeCoNi HEAs [27], all of which include the element of Co. Figure 3b shows the corresponding strain hardening rate. Another parameter used for evaluating strain hardening capability is the strain hardening exponent n, whose value could be simulated by the Hollomon and Ludwick equations, respectively, as shown below [28]:

$$\sigma = K\varepsilon_p^n \tag{3}$$

$$\sigma = \sigma_0 + K\varepsilon_p^n \tag{4}$$

where σ is true stress; σ_0 is the yield strength; ε_p is true strain; and K is a strength coefficient representing the true stress when $\varepsilon_p = 1$. Figure 3 shows engineering and true stress–strain curves of $Fe_{50}Mn_{20}Cr_{20}Ni_{10}$ MEA and Fig. 4 is the simulated curves by Hollomon and Ludwick equations. Table 3 lists the simulated values of n, K and σ_0 from Hollomon and Ludwick equations. The overall n of $Fe_{50}Mn_{20}Cr_{20}Ni_{10}$ MEA is 0.41 by the Hollomon equation and

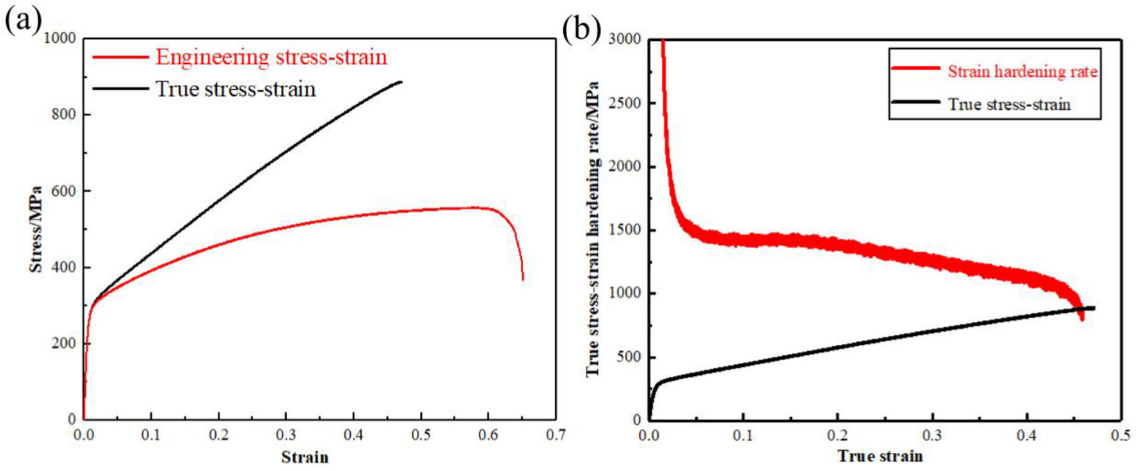

Fig. 3 Mechanical properties of $Fe_{50}Mn_{20}Cr_{20}Ni_{10}$ alloy at room temperature. **a** Tensile engineering and true stress–strain curves; **b** strain hardening rate Θ versus true strain

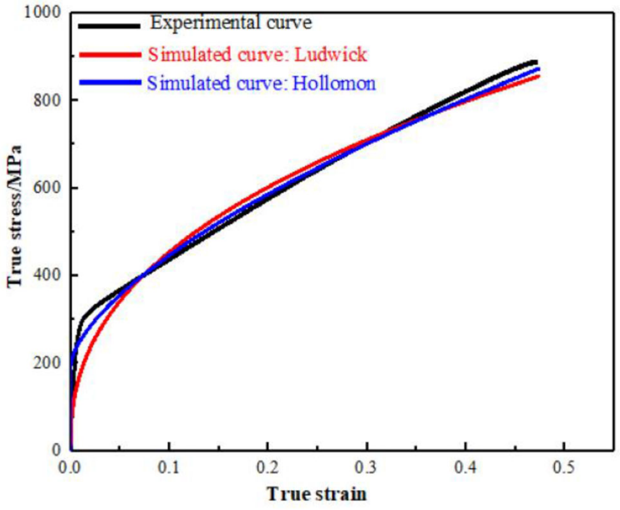

Fig. 4 Experimental true stress–strain curves of $Fe_{50}Mn_{20}Cr_{20}Ni_{10}$ MEA and simulated curves by Hollomon ($\sigma = K\varepsilon_p^n$) and Ludwick ($\sigma = \sigma_0 + K\varepsilon_p^n$) equations

Table 3 Simulated values of n, K and σ_0 from Hollomon and Ludwick equations

Sample	Elongation/%	Hollomon		Ludwick		
		K/MPa	n	σ_0/MPa	K/MPa	n
HEA	0–47	1160	0.41	193	1091	0.63

0.63 by the Ludwick equation. The high value of n indicates a high strain hardening ability for the current $Fe_{50}Mn_{20}Cr_{20}Ni_{10}$ MEA, which are superior values among HEAs as well as TWIP and TRIP alloys [29–31]. It is reasonable that the flow stress will remarkably increase, since the newly formed twins refine the grain size and introduce new interface obstacles. Therefore, the strain hardening behavior from twinning is known as a dynamic Hall–Petch effect. Based on Hart's theory [32] and the Considère criterion [33], strain hardening rate $\left(\Theta = \frac{d\sigma}{d\varepsilon}\right)$ contributed to high ductility, as it can help delay necking and maintain elongation. Consequently, the uniform elongation of $Fe_{50}Mn_{20}Cr_{20}Ni_{10}$ alloy is comparable to that of other alloys and MEAs/HEAs [2, 19, 24, 25].

3.4 Prediction of yield strength

According to classical Labush model [36] for concentrated solid solutions, already successfully applied to HEAs [37], solid solution strengthening (SSS) caused by the atoms of i element ($\Delta\sigma_{SSi}$) can be described as:

$$\Delta\sigma_{SSi} = ZGf_i^{4/3}C_i^{2/3} \tag{5}$$

where G is the shear modulus of the alloy, 81.8 GPa; Z is a fitting constant; C_i is the concentration of element i; r_i and G_i are i-atomic size and shear modulus; and f_i is the mismatch parameter, which can be calculated using the following formula:

$$f_i = \left(\delta G_i^2 + \alpha^2\delta r_i^2\right)^{1/2} \tag{6}$$

where $\delta r_i = \left(\frac{1}{r}\right)dr/dC_i$ and $\delta G_i = \frac{1}{G}dG/dC_i$ are atomic size and the atomic modulus mismatch parameters, respectively; and α is a constant dependent on the type of the mobile dislocations. Generally, α is 2–4 for the screw dislocations and $\alpha \geq 16$ for edge dislocations [38].

The mismatch parameters δG_i and δr_i can be estimated in accordance with the method proposed in Refs. [38, 39]. In an FCC lattice, each element has 12 nearest-neighbor atoms, thus forming a 13-atom cluster. If the local environment around the alloying element i is assumed to be equal to the average composition of the alloy, element i has

$N_j = 13C_j$ of j-atom and $N_i = 13\ C_i - 1$ of i-atom neighbors ($j \neq i$). Then, δr_i and δG_i mismatches in the vicinity of the element i are estimated as an average of the atomic size difference, $\delta r_{ij} = 2\left(r_i - r_j\right)/\left(r_i + r_j\right)$ and shear modulus difference, $\delta G_{ij} = 2\left(G_i - G_j\right)/\left(G_i + G_j\right)$, respectively, of this element with its neighbors:

$$\delta r_i = \frac{13}{12}\sum C_j \delta r_{ij} \qquad (7)$$

$$\delta G_i = \frac{13}{12}\sum C_j \delta G_{ij} \qquad (8)$$

The calculated values of δr_i and δG_i for different constituent elements of $Fe_{50}Mn_{20}Cr_{20}Ni_{10}$ alloy calculated using Eqs. (7) and (8) are given in Table 4. Apparently, the highest (absolute) atomic size mismatches, δr_i, in the $Fe_{50}Mn_{20}Cr_{20}Ni_{10}$ alloy are around Cr and Ni atoms of 0.0520 and − 0.0650, respectively. Likewise, the highest atomic modulus mismatches in $Fe_{50}Mn_{20}Cr_{20}Ni_{10}$ alloy are around Cr and Ni atoms of 0.3009 and − 0.1434, respectively. It should be noted that the absolute value of δG_{Cr} is more than twice higher than the value of $\delta G_{Ni.}$

f_i values are calculated using Eq. (6) with α value of 2. Calculations were performed with an assumption that $Fe_{50}Mn_{20}Cr_{20}Ni_{10}$ alloy is single solid solution phase with a composition corresponding to nominal composition of the alloy. Obviously, the mismatch parameter for Cr is significantly higher than those for other constitutive elements.

$\Delta\sigma_{SSi}$ is calculated using Eq. (5), Z value is 0.04 and G value is 81.8 GPa. $\Delta\sigma_{SSCr}$ is distinctly higher than solid solution strengthening by other elements: $\Delta\sigma_{SSNi}$ is 79.92 MPa, while $\Delta\sigma_{SSFe}$ and $\Delta\sigma_{SSMn}$ are 18.18 and 41.62 MPa, respectively. It should be noted that $\Delta\sigma_{SSCr}$ = 246.30 MPa, and $\Delta\sigma_{SSNi}$ is only approximately 32% of $\Delta\sigma_{SSCr}$, whereas $\Delta\sigma_{SSFe}$ and $\Delta\sigma_{SSMn}$ are about 7% and about 17% of $\Delta\sigma_{SSCr}$, respectively. This analysis reveals that SSS by single element (Cr) with atomic fraction of 20% is about 1.8 times higher than strengthening by other elements. Therefore, the conclusion can be applied to complexly concentrated multi-component alloys, in which, only certain elements can produce strong SSS effect, while other constitutive elements only slightly strengthen alloys.

SSS effect in multi-component alloys can be calculated using the Gypen and Deruyttere methods [40] that have been successfully applied to HEA [37]. In this way, overall solid solution strengthening of alloy, $\Delta\sigma_{SS}$, can be calculated using the following formula by summarizing the $\Delta\sigma_{SSi}$ of each component in the alloy:

$$\Delta\sigma_{SS} = \left(\sum_i \Delta\sigma_{SSi}^{3/2}\right)^{2/3} \qquad (9)$$

Table 4 Calculated lattice, δr_i, and shear modulus, δG_i, distortions near an individual constituent element i in $Fe_{50}Mn_{20}Cr_{20}Ni_{10}$ alloy

Parameter	Fe	Mn	Cr	Ni
δr_i	−0.0153	0.0189	0.0520	−0.0650
δG_i	−0.0617	−0.0749	0.3009	−0.1434

The calculated values of $\Delta\sigma_{SS}$ of $Fe_{50}Mn_{20}Cr_{20}Ni_{10}$ MEA are plotted against the experimental values of the corresponding alloys in Fig. 5. A good fit between the calculated values of $\Delta\sigma_{SS}$ and experimentally determined yield strength (YS) of the alloys is reached. The reason for the slight difference between the predicted yield strength and experimental value is that the mechanical behavior of MEAs is directly correlated with the degree of local chemical order [42, 43]. The correlation between the predicted SSS and experimental yield strength illustrates two following facts: (i) the methodology developed for predicting SSS in conventional alloys, i.e., Labush approach and Gypen and Deruyttere approach, is working for MEAs or HEAs if contributions from each constitutive element of the alloys are estimated and summarized; (ii) the yield strength of the solid solution alloys can be primarily attributed to SSS.

3.5 Deformation mechanisms

The deformation behavior of metals mainly includes dislocation multiplication and interactions between dislocations and other crystal defects as well as themselves. According to the classic Taylor hardening model [44], the quantitative forest hardening effect of dislocations in $Fe_{50}Mn_{20}Cr_{20}Ni_{10}$ MEA is given by:

$$\Delta\sigma = M\alpha Gb\sqrt{\rho} \qquad (10)$$

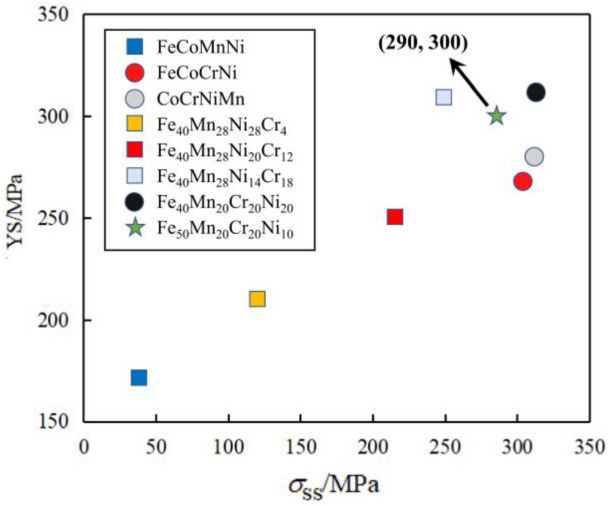

Fig. 5 Dependence of YS on $\Delta\sigma_{SS}$ of studied Fe-based MEA alloys and some quaternary equiatomic alloys reported in Refs. [19, 41, 50]

where $\Delta\sigma$ is the corresponding increase in the tensile stress; M is the Taylor factor, 3.06; b is the magnitude of the Burgers vector (0.253 nm); and ρ is the dislocation density. α is 0.2 in Eq. (10). The actual value of α is determined by the geometrical arrangement of the dislocation, and it decreases continuously with plastic deformation. However, the variations are in a 10% range [45], and thus it is approximated as a stable constant during the plastic deformation. Here, it is assumed that if no accumulation of dislocations occurs when yields, then, σ can be obtained by the corresponding ρ at different tensile strains as $\sigma = \Delta\sigma + \mathrm{YS}$. The difference between the calculated and experimental flow stress is increased with straining, since the contribution of stacking faults and twins is not considered. In general, the forest dislocation hardening effect is the major mechanism in the initial deformation stage in $Fe_{50}Mn_{20}Cr_{20}Ni_{10}$ MEA.

The variation in strength, ductility and strain hardening with Mn content is closely related to the deformation mechanisms. An essential novelty of the current finding is the fact that the newly designed $Fe_{50}Mn_{20}Cr_{20}Ni_{10}$ alloy shows deformation-induced nano-twins at room temperature. It has been reported that the equiatomic $Fe_{20}Mn_{20}Ni_{20}Co_{20}Cr_{20}$ HEA exhibited deformation twinning only at 77 K [11]. For FCC HEAs, it has been reported that the main deformation mechanism is the dislocation slip at room temperature, although it changes to the deformation twinning at cryogenic temperature as the resolved shear stress is sufficient to reach the critical stress for twinning [46]. In order to explore the deformation mechanisms at room temperature, the presence of the deformation twins is further confirmed by TEM analysis, as shown in Fig. 6a. The high-density dislocations accumulated within deformation twin and the corresponding selected area electron diffraction (SAED) pattern are presented in Fig. 6b–d, where the activated twin system was indexed as $[\bar{1}12](1\bar{1}1)$, similar to a compound FCC twin commonly observed in FCC crystalline alloys [47].

Now, it is widely accepted that twinning during deformation continuously increases new interfaces that promote work hardening by decreasing the dislocation mean-free path [48]. It is commonly referred as the "dynamic Hall–Petch" effect. In addition, the triggered deformation twins at cryogenic temperature and/or high strain rate contain high-density dislocations that act as strong barriers to dislocation glides, which further primarily contributes to strain hardening [49–53]. Hence, the improvement in the strength mainly by the activation of nano-twins is quite significant. The formation of more complex planar dislocation configurations is available, such as dislocation walls and dislocation networks (Fig. 6e). It should be noted that the formation of dislocation networks enables the transformation of dislocation pile-up into planar dislocation structures in Ref. [24]. Figure 6f symbolically shows the deformation mechanisms of the alloy under the joint action of dislocation cells, dislocation walls and deformation twins. Therefore, the mechanical properties of the present Fe-based MEA are better than those in many other major HEA classes.

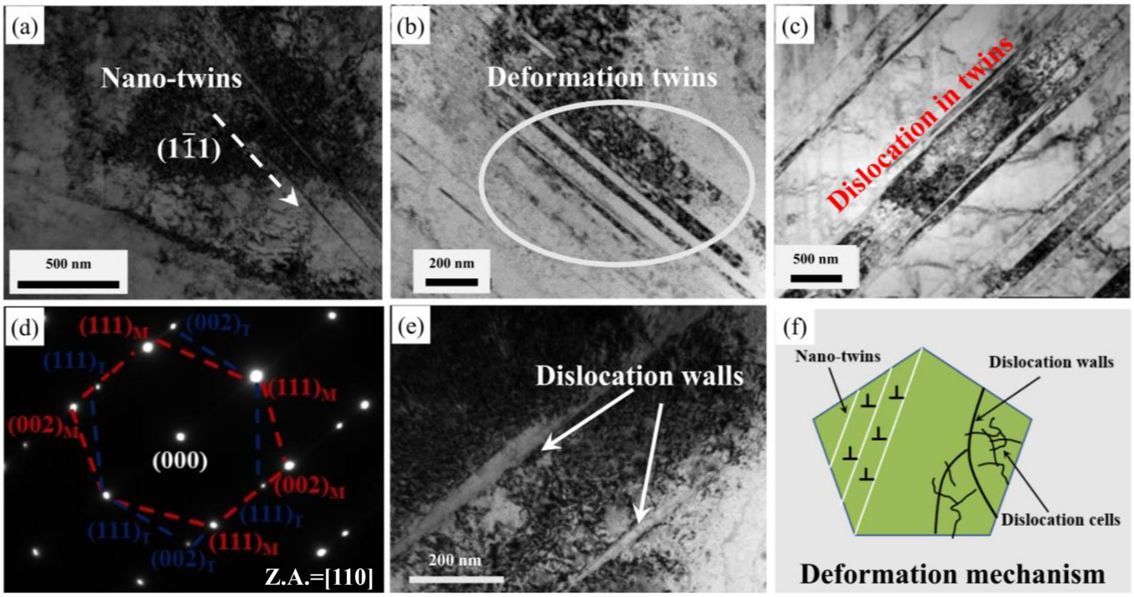

Fig. 6 TEM images on [110] zone axis (Z.A.) of tensile-fractured Fe-MEA with ε = 60%. **a** Dark field image showing deformation nano-twinning system in Fe-MEA; **b**, **c** bright field images of high-density dislocations within twins; **d** corresponding SAED pattern of matrix (M) and twin (T); **e** high-density dislocations accumulated between dislocation walls; **f** schematic sketch illustrating deformation mechanism in Fe-MEA

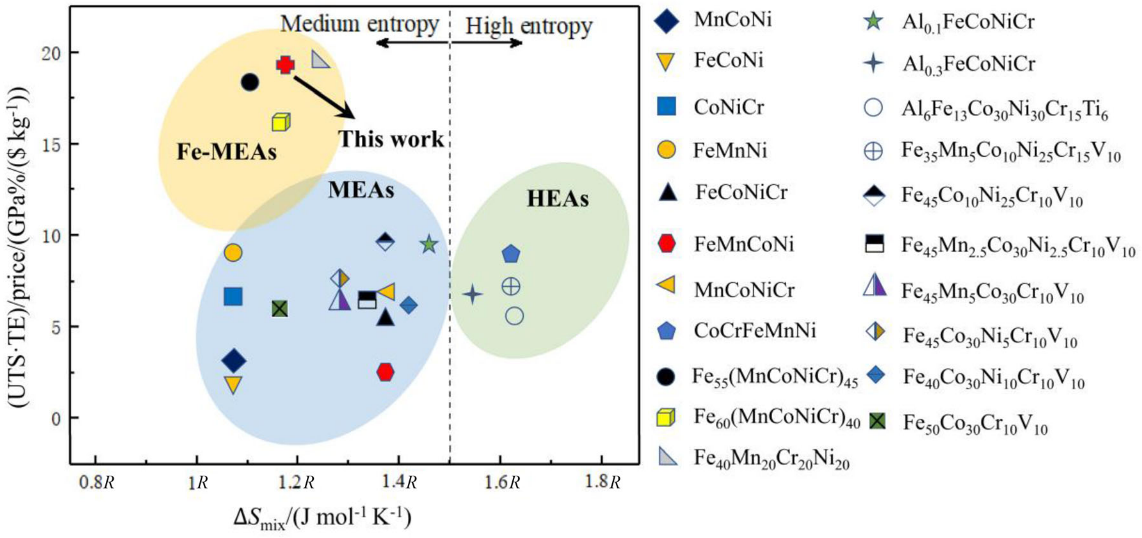

Fig. 7 UTS·TE/price ratio versus configurational entropy of Fe-MEAs in comparison with other previously developed HEAs and MEAs [19, 54, 55]

The design strategy, mechanical properties and deformation mechanism of Fe-based MEA are discussed in detail above. It can be found that the design concept of Fe-based MEA combines the advantages of TWIP steels and HEAs. Figure 7 shows that Fe-MEA concept is a potential guide for the development of low-cost, but high-performance HEAs or MEAs. It summarizes (UTS·TE/price) versus configurational entropy of Fe-MEAs in comparison with other previously developed HEAs and/or MEAs where R is gas constant, 8.314 J mol^{-1} K^{-1}, UTS is ultimate tensile strength, GPa; and TE is total elongation to fracture, %. Obviously, compared to many Co-containing HEAs or MEAs, Fe-based MEAs have very broad development aspect and application prospects. The successful design of Fe-based MEAs greatly promoted the development of new alloys with low cost and excellent mechanical performance, which will be the critical point for alloy design and practical industry application in the future.

4 Conclusions

1. The mechanical properties of $Fe_{50}Mn_{20}Cr_{20}Ni_{10}$ MEA were comparable to the equiatomic CoCrFeMnNi alloy due to the deformation twins. The average strain hardening exponents simulated by the Hollomon equation and the Ludwick equation were 0.41 and 0.63, respectively.
2. The solid solution strengthening caused by different elements of $Fe_{50}Mn_{20}Cr_{20}Ni_{10}$ MEA was calculated using Labush approach. It shows that Cr produces strongest solid solution strengthening among the constitutive elements of the alloys. According to the Gypen and Deruyttere method, the contribution of each element of the alloy is summarized to evaluate the solid solution strengthening of $Fe_{50}Mn_{20}Cr_{20}Ni_{10}$ MEA. A good correlation between the experimental yield strength value and the predicted solid solution strengthening was observed.
3. The forest dislocation hardening effect, calculated by the Taylor hardening model, and a dynamic Hall–Petch effect caused by deformation twins were the primary hardening contributor during the plastic deformation.
4. Compared with other major HEA classes, the present Fe-MEA has outstanding combination mechanical properties and low cost, providing a new direction for future development of HEAs and MEAs.

Acknowledgements The authors would like to acknowledge the financial support of the Natural Science Foundation of Shanxi Province, China (Nos. 201901D111105 and 201901D111114), Transformation of Scientific and Technological Achievements Programs of Higher Education Institutions in Shanxi (2019), State Key Lab of Advanced Metals and Materials of China (Grant No. 2020-Z09), and the opening project of the State Key Laboratory of Explosion Science and Technology (Beijing Institute of Technology), and the opening project number is KFJJ20-13M.

References

[1] J.W. Yeh, S.K. Chen, S.J. Lin, J.Y. Gan, T.S. Chin, T.T. Shun, C.H. Tsau, S.Y. Chang, Adv. Eng. Mater. 6 (2004) 299–303.
[2] B. Cantor, I.T.H. Chang, P. Knight, A.J.B. Vincent, Mater. Sci. Eng. A 375–377 (2004) 213–218.
[3] Y. Zhang, T.T. Zuo, Z. Tang, M.C. Gao, K.A. Dahmen, P.K. Liaw, Z.P. Lu, Prog. Mater. Sci. 61 (2014) 1–93.
[4] Y. Ye, Q. Wang, J. Lu, C. Liu, Y. Yang, Mater. Today 19 (2016) 349–362.

[5] M.H. Tsai, J.W. Yeh, Mater. Res. Lett. 2 (2014) 107–123.
[6] Z. Li, K.G. Pradeep, Y. Deng, D. Raabe, C.C. Tasan, Nature 534 (2016) 227–230.
[7] O.N. Senkov, G.B. Wilks, J.M. Scott, D.B. Miracle, Intermetallics 19 (2011) 698–706.
[8] Z.Y. Ding, Q.F. He, Q. Wang, Y. Yang, Int. J. Plasticity 106 (2018) 57–72.
[9] K.S. Ming, X.F. Bi, J. Wang, Int. J. Plasticity 100 (2018) 177–191.
[10] C.C. Tasan, Y. Deng, K.G. Pradeep, M.J. Yao, H. Springer, D. Raabe, JOM 66 (2014) 1993–2001.
[11] B. Gludovatz, A. Hohenwarter, D. Catoor, E.H. Chang, E.P. George, R.O. Ritchie, Science 345 (2014) 1153–1158.
[12] F. Otto, A. Dlouhý, C. Somsen, H. Bei, G. Eggeler, E.P. George, Acta Mater. 61 (2013) 5743–5755.
[13] A. Saeed-Akbari, L. Mosecker, A. Schwedt, W. Bleck, Metall. Mater. Trans. A 43 (2012) 1688–1704.
[14] S. Allain, J.P. Chateau, O. Bouaziz, S. Migot, N. Guelton, Mater. Sci. Eng. A 387–389 (2004) 158–162.
[15] V. Shterner, I.B. Timokhina, H. Beladi, Mater. Sci. Eng. A 669 (2016) 437–446.
[16] S. Curtze, V.T. Kuokkala, Acta Mater. 58 (2010) 5129–5141.
[17] A.J. Zaddach, C. Niu, C.C. Koch, D.L. Irving, JOM 65 (2013) 1780–1789.
[18] K.H. Lo, C.H. Shek, J.K.L. Lai, Mater. Sci. Eng. R Rep. 65 (2009) 39–104.
[19] B.B. Bian, N. Guo, H.J. Yang, R.P. Guo, L. Yang, Y.C. Wu, J.W. Qiao, J. Alloy. Compd. 827 (2020) 153981.
[20] O. Dmitrieva, D. Ponge, G. Lnden, J. Millán, P. Choi, J. Sietsma, D. Raabe, Acta Mater. 59 (2011) 364–374.
[21] D. Raabe, S. Sandlöbes, J. Millán, D. Ponge, H. Assadi, M. Herbig, P.P. Choi, Acta Mater. 61 (2013) 6132–6152.
[22] M. Kuzmina, D. Ponge, D. Raabe, Acta Mater. 86 (2015) 182–192.
[23] M.J. Yao, K.G. Pradeep, C.C. Tasan, D. Raabe, Scripta Mater. 72–73 (2014) 5–8.
[24] Y. Deng, C.C. Tasan, K.G. Pradeep, H. Springer, A. Kostka, D. Raabe, Acta Mater. 94 (2015) 124–133.
[25] Z.M. Li, F. Körmann, B. Grabowski, J. Neugebauer, D. Raabe, Acta Mater. 136 (2017) 262–270.
[26] Z.M. Li, C.C. Tasan, H. Springer, B. Gault, D. Raabe, Sci. Rep. 7 (2017) 40704.
[27] Z.G. Wu, Y.F. Gao, H.B. Bei, Acta Mater. 120 (2016) 108–119.
[28] T.H. Courney, in: Mechanical Behavior of Materials, 2nd ed., McGraw-Hill, New York, USA, 2000.
[29] X.L. Wu, M.X. Yang, F.P. Yuan, L. Chen, Y.T. Zhu, Acta Mater. 112 (2016) 337–346.
[30] M.M. Wang, C.C. Tasan, D. Ponge, D. Raabe, Acta Mater. 111 (2016) 262–272.
[31] Z.C. Li, R.D.K. Misra, Z.H. Cai, H.X. Li, H. Ding, Mater. Sci. Eng. A 673 (2016) 63–72.
[32] E.W. Hart, Acta Metall. 15 (1967) 351–355.
[33] Q. Wei, S. Cheng, K.T. Ramesh, E. Ma, Mater. Sci. Eng. A 381 (2004) 71–79.
[34] X. Yang, Y. Zhang, Mater. Chem. Phys. 132 (2012) 233–238.
[35] R.T. Chen, G. Qin, H.T. Zheng, L. Wang, Y.Q. Su, Y.L. Chiu, H.S. Ding, J.J. Guo, H.Z. Fu, Acta Mater. 144 (2018) 129–137.
[36] R. Labusch, Phys. Status Solidi 41 (1970) 659–669.
[37] I. Toda-Caraballo, P.E.J. Rivera-Díaz-del-Castillo, Acta Mater. 85 (2015) 14–23.
[38] O.N. Senkov, J.M. Scott, S.V. Senkova, D.B. Miracle, C.F. Woodward, J. Alloy. Compd. 509 (2011) 6043–6048.
[39] G.A. Salishchev, M.A. Tikhonovsky, D.G. Shaysultanov, N.D. Stepanov, A.V. Kuznetsov, I.V. Kolodiy, A.S. Tortika, O.N. Senkov, J. Alloy. Compd. 591 (2014) 11–21.
[40] L.A. Gypen, A. Deryuttere, J. Mater. Sci. 12 (1977) 1028–1033.
[41] N.D. Stepanov, D.G. Shaysultanov, M.A. Tikhonovsky, G.A. Salishchev, Mater. Des. 87 (2015) 60–65.
[42] Y. Ma, Q. Wang, C. Li, L.J. Santodonato, M. Feygenson, C. Dong, P.K. Liaw, Scripta Mater. 144 (2018) 64–68.
[43] R. Zhang, S. Zhao, J. Ding, Y. Chong, T. Jia, C. Ophus, M. Asta, R.O. Ritchie, A.M. Minor, Nature 581 (2020) 283–287.
[44] J.K. Kim, B.C. De Cooman, Mater. Sci. Eng. A 676 (2016) 216–231.
[45] W. Püschl, Prog. Mater. Sci. 47 (2002) 415–461.
[46] G. Laplanche, A. Kostka, O.M. Horst, G. Eggeler, E.P. George, Acta Mater. 118 (2016) 152–163.
[47] N.L. Okamoto, S. Fujimoto, Y. Kambara, M. Kawamura, Z.M.T. Chen, H. Matsunoshita, K. Tanaka, H. Inui, E.P. George, Sci. Rep. 6 (2016) 35863.
[48] O. Bouaziz, S. Allain, C. Scott, Scripta Mater. 58 (2008) 484–487.
[49] H. Idrissi, K. Renard, D. Schryvers, P.J. Jacques, Scripta Mater. 63 (2010) 961–964.
[50] Z. Yang, M. Yang, Y. Ma, L. Zhou, W. Cheng, F. Yuan, X. Wu, Mater. Sci. Eng. A 793 (2020) 139854.
[51] Y. Ma, F. Yuan, M. Yang, P. Jiang, E. Ma, X. Wu, Acta Mater. 148 (2018) 407–418.
[52] Z. Li, S. Zhao, S.M. Alotaibi, Y. Liu, B. Wang, M.A. Meyers, Acta Mater. 151 (2018) 424–431.
[53] Z. Li, S. Zhao, H. Diao, P.K. Liaw, M.A. Meyers, Sci. Rep. 7 (2017) 42742.
[54] J.W. Bae, H.S. Kim, Scripta Mater. 186 (2020) 169–173.
[55] J.W. Bae, J.B. Seol, J. Moon, S.S. Sohn, M.J. Jang, H.Y. Um, B.J. Lee, H.S. Kim, Acta Mater. 161 (2018) 388–399.